J Mater Sci: Mater Med (2018) 29:11
DOI 10.1007/s10856-017-6020-6

S.I.: BIOFABRICATION AND BIOINKS FOR TISSUE ENGINEERING

Original Research

# Bioactive calcium silicate/poly-ε-caprolactone composite scaffolds 3D printed under mild conditions for bone tissue engineering

**Yen-Hong Lin[1,2] · Yung-Cheng Chiu[3,4] · Yu-Fang Shen[5,6] · Yuan-Haw Andrew Wu[2,3] · Ming-You Shie[2,5,7]**

Received: 4 November 2017 / Accepted: 5 December 2017 / Published online: 27 December 2017


**Abstract** The present study provides a solvent-free processing method for establishing the ideal porous 3-dimension (3D) scaffold filled with different ratios of calcium silicate-based (CS) powder and polycaprolactone (PCL) for 3D bone substitute application. Characterization of hybrid scaffolds developed underwent assessments for physicochemical properties and biodegradation. Adhesion and growth of human Wharton's Jelly mesenchymal stem cells (WJMSCs) on the CS/PCL blended scaffold were investigated *in vitro*. Cell attachment and morphology were examined by scanning electron microscope (SEM) and confocal microscope observations. Colorimetric assay was tested for assessing cell metabolic activity. In addition, RT-qPCR was also performed for the osteogenic-related and angiogenesis-related gene expression. As a result, the hydrophilicity of the scaffolds was further significantly improved after we additive CS into PCL, as well as the compressive strength up to 5.8 MPa. SEM showed that a great amount of precipitated bone-like apatite formed on the scaffold surface after immersed in the simulated body fluid. The 3D-printed scaffolds were found to enhance cell adhesion, proliferation and differentiation. Additionally, results of osteogenesis and angiogenesis proteins were expressed obviously greater in the response of WJMSCs. These results indicate the CS/PCL composite exhibited a favorable bioactivity and osteoconductive properties that could be served as a promising biomaterial for bone tissue engineering scaffolds.

## 1 Introduction

Bone substitutes have had increased demands within recent years due to the drastic increase in incidence of bone-related diseases in aging societies. The choice of materials and method of manufacturing of these bone substitutes need to be carefully studied in order to manufacture bone substitutes that have optimal biocompatibility at tissue and organ level while maintaining sufficient mechanical strength [1]. There are various techniques and several biomaterials currently available for these purpose, such as autologous bone, allograft bone, xenograft bone, bioceramics such as tricalcium phosphate, polycaprolactone [2]. Each biomaterial has advantages and disadvantages, and the search for an optimal material continues.

Polymers including PCL, PLGA, PLA, etc. have been commonly mixed with ceramic biomaterials for hard tissue engineering [3–6]. Of these biocompatible polymers,

Yen-Hong Lin and Yung-Cheng Chiu contributed equally to this work.

✉ Ming-You Shie
eric@mail.cmu.edu.tw

1 The Ph.D. program for Medical Engineering and Rehabilitation Science, China Medical University, Taichung, Taiwan

2 3D Printing Medical Research Center, China Medical University Hospital, Taichung, Taiwan

3 School of Medicine, China Medical University, Taichung City, Taiwan

4 Department of Orthopedics, China Medical University Hospital, Taichung City, Taiwan

5 Department of Bioinformatics and Medical Engineering, Asia University, Taichung, Taiwan

6 3D Printing Research Center, Asia University, Taichung, Taiwan

7 School of Dentistry, China Medical University, Taichung, Taiwan

polycaprolactone (PCL) has the lowest melting point, making the material itself malleable and 3D printable at a temperature that can be easily achieved in lab settings [7]. PCL also has very resilient physical properties that closely resemble those of many hard tissues. However, despite its excellent mechanical strength and FDA-approved biocompatibility, PCL is limited in its biomedical application due to its polyester molecular structure that causes hydrophobicity. This drawback of PCL is commonly overcome by mixing it with another ceramic material to endow the resulting composite a significant degree of hydrophilicity [8]. Ceramics, such as calcium phosphate or calcium silicate (CS)-based biomaterials have been popularly used in the fabrication of bone substitutes, as these materials, collectively known as bone cement, have excellent biocompatibility [7, 9]. Calcium silicate-based material has been widely used in bone substitution due to its outstanding bioactive properties. In fact, our previous studies have shown that CS-based materials have the ability to produce a calcified bone-like apatite layer that already comprises phosphate. The apatite-rich surface layer is precipitated when it immersing in simulated body fluid. Our group has also successfully demonstrated the extraordinary biodegradability and osteoconductivity of CS. Other recent *in vivo* and *in vitro* experiments have also shown that the ion release kinetics of calcium-silicate-based materials harnessed excellent osteogenesis and odontogenesis results, supporting the attachment, proliferation, and differentiation of various types of stem cells [10–12]. The released Ca ions can bring to systemic calcium ion homeostasis, and induce some bone gene expression like bone morphogenetic protein-2 (BMP-2) [13]. In process of bone metabolism, it can act on human mineralizing cells such as human mesenchymal stem cells (hMSCs) and human dental pulp cells (hDPCs), promoting osteoblast proliferation, differentiation, and extracellular matrix mineralization. On the other hand, the capacity of Si ions can promote the calcification of bone tissue, stimulating osteogenic differentiation and angiogenesis. Si had also found not only adsorb various bone-tissue-related ECM components but also involved the up-regulation of MAPK/ERK and MAPK/p38 signalling pathway [14–16].

3D printing, formally known as additive manufacturing, has the ability to produce products from any customizable CAD files processed from magnetic resonance imaging, computed tomography, or any other imaging capturing methods [17, 18]. This characteristic of 3D printing allows the production of personalized scaffolds. Bone substitutes may effectively enhance hard tissue regeneration by incorporating pores into them [19]. The layer-by-layer manufacturing method of 3D printing not only can produce scaffolds of high porosity traits, but it also allows the full interconnectivity of these miniature pores of precise measurements, which is nearly impossible to achieve by means of traditional scaffold manufacturing, including electrospinning, polyurethane foam, porogen templating, solvent casting, and freeze drying [20–22]. These interconnected pores are indispensable for bone tissue engineering as they support full in-growth of tissue and vessel sprouts during angiogenesis throughout the tissue growth/regeneration process [23].

In this study, we fabricated 3D printed scaffolds contained various different concentration of CS ceramic powder and proven the 3D printing parameters used to produce porous scaffolds for bone tissue engineering. The extent of cellular adhesion, proliferation, and osteogenesis of these bioscaffolds were tested with human Wharton's Jelly mesenchymal stem cells (WJMSC).

## 2 Materials and methods

### 2.1 CS powder preparation

The method used here for the preparation of the CS powder has been described elsewhere [24]. In brief, reagent grade CaO (Sigma-Aldrich, St. Louis, MO), $SiO_2$ (High Pure Chemicals, Saitama, Japan) and MgO (Sigma-Aldrich) powders were used as matrix materials (composition: 65% CaO, 25% $SiO_2$, and 10% MgO). The oxide mixtures were then sintered at 1400 °C for 2 h using a high-temperature furnace. The CS powder was ball-milled in 99.5% ethanol in a centrifugal ball mill (S100, Retsch, Hann, Germany) for 6 h and dried at 100 °C for 6 h.

### 2.2 Preparation of the CS/PCL paste

CS powder was immersed in 99.5% ethanol and stirred at 400 rpm overnight. The homogenously dissolved CS in ethanol was slowly added into molten PCL beads (Mw = 43,000–50,000, Polysciences, Warrington, PA) and stirred with a metal rod at 200 °C until the CS-ethanol solution was evenly mixed with the PCL to create a CS/PCL paste. After mixing, the paste was left in the oven at 85 °C for 1 day. In this study, the specimens coded as 'CS0', 'CS10', 'CS30' and 'CS50' represent the specimen means of 0% CS/100% PCL, 10% CS/90% PCL, 30% CS/70% PCL and 50% CS/50% PCL, respectively.

### 2.3 Scaffold fabrication

The CS/PCL 3D scaffolds were manufactured with a BioScaffolder (BioScaffolder 3.1, GeSiM, Großerkmannsdorf, Germany). The CS/PCL paste was transferred into the printing cartridge with a 20 G nozzle. The printing speed was 2 mm/s under 450 kPa of extrusion pressure. The

3D-scaffold measured 6.5 mm × 6.5 mm × 6.5 mm. After printing, the scaffold was allowed to dry at room temperature for 2 h. The strut with a diameter of 500 μm were printed in parallel with a gap of 500 μm between the struts. Subsequent layers were printed at an angle of 90° with the underlying layer.

### 2.4 Characterization

The water contact angle for each scaffold was considered at room temperature. Briefly, the scaffolds were placed on the top of a stainless-steel base; a drop of 20 μL Dulbecco's modified Eagle medium (DMEM; Caisson, North Logan, UT, USA) was placed on the surface of the scaffolds, and an image was taken with a camera after 20 min had elapsed. The resulting images were analyzed using ImageJ (National Institutes of Health) to determine the water contact angle. The phase composition of the cements was analyzed using X-ray diffractometry (XRD; Bruker D8 SSS, Karlsruhe, Germany) run at 30 kV and 30 mA at a scanning speed of 1°/min. In addition, the CS content of the scaffolds was determined by thermogravimetric analysis (TGA, Netzsch STA 449C, Bavaria, Germany). The samples were analyzed in aluminum pans under a nitrogen purge and heated from 100 to 700 °C with a heating rate of 10 °C/min. Finally, the compressive strength of the scaffolds was measured on an EZ-Test machine (Shimadzu, Kyoto, Japan) at a loading rate of 1 mm/min. The maximum compressive load at failure was obtained from the recorded load-deflection curves. Three independent measurements were carried out and the data were expressed as mean ± SD.

### 2.5 In vitro soaking

The scaffolds were soaked in a simulated body fluid (SBF) solution at 37 °C. The SBF solution was similar to ionic components in human blood plasma and consisted of 7.9949 g of NaCl, 0.2235 g of KCl, 0.147 g of $K_2HPO_4$, 0.3528 g of $NaHCO_3$, 0.071 of g $Na_2SO_4$, 0.2775 g of $CaCl_2$ and 0.305 g of $MgCl_2{\cdot}6H_2O$ in 1000 mL of distilled $H_2O$. The pH was adjusted to 7.4 with hydrochloric acid and trishydroxymethyl aminomethane (Tris). After soaking for different time periods, the scaffolds were removed from SBF, washed with distilled water, and investigated the weight loss and microstructure of the scaffolds. The degree of degradation was determined by monitoring the weight change of the scaffolds. After drying for 1 day, the scaffolds were weighed both before and after immersion using a balance (TE214S, Sartorius, Goettingen, Germany). Ten specimens were examined for each of the materials investigated at each time point. Then, the specimens were coated with gold and their morphologies were investigated under a scanning electron microscope (SEM; JSM-6700F, JEOL) operated in the lower secondary electron image (LEI) mode at 3 kV accelerating voltage.

### 2.6 Cell proliferation

Before performing the cell experiments, all scaffolds were sterilized by being immersed in 75% ethanol and exposed to ultraviolet light for 15 min. The human Wharton's Jelly mesenchymal stem cells (WJMSCs) were obtained from the Bioresource Collection and Research Center (BCRC, Hsin-Chu, Taiwan) and grown in a mesenchymal stem cell medium (Sciencell) to passage 3–6. The WJMSCs were directly cultured on the scaffolds at a density of $5 \times 10^4$ cells per well in a DMEM-filled 48-well plate and incubated at 37 °C in a 5% $CO_2$ atmosphere for various durations. After different culturing, the cell viability was considered using the PrestoBlue® (Invitrogen, Grand Island, NY) assay. At the end of the culture period, the DMEM was removed, and the wells were washed twice with cold PBS. Then, each well with a specimen was filled with PrestoBlue® and fresh DMEM at a ratio of 1:9 and incubated at 37 °C for 60 min. The resulting solution in each well was then transferred to a new 96-well plate, and the optical density (OD) of the solutions was measured using Tecan Infinite 200® PRO microplate reader (Tecan, Männedorf, Switzerland) at 570 nm with a reference wavelength of 600 nm. The results were obtained in triplicate from three separate experiments. The cell cultured on tissue culture plates without scaffolds were used as a control (Ctl).

### 2.7 Fluorescent staining

We observed the cell morphology of WJMSCs after culturing on scaffold using F-actin cytoskeleton stains. After incubation for 1 day, the cells were washed with PBS, fixed in 4% paraformaldehyde (Sigma-Aldrich) at room temperature for 20 min, and then permeabilized with PBS containing 0.1% Triton X-100 (Sigma). The F-actin filaments were stained with phalloidin conjugated to Alexa Fluor 594 (Invitrogen) for 1 h. The nuclei were stained with 300 nM DAPI (Invitrogen) for 30 min. After washing, the morphology was obtained using a white light laser confocal microscope (Leica TCS SP8, Wetzlar, Germany).

### 2.8 Osteogenesis and angiogenesis assay

In this study, we consider the osteogenic-, and angiogenic-related genes (ALP, OPN, OC, vWF and Ang-1), of WJMSC after being cultured for 7 days. Total RNA of all five groups was extracted using TRIzol reagent (Invitrogen) and analyzed using RT-qPCR. Total RNA (500 ng) was used for the synthesis of complementary DNA using a cDNA Synthesis Kit (GeneDireX) following the

**Table 1** Primer pairs used in this study

| Gene | Sequence |
|---|---|
| ALP | Forward: 5′-ATCTTTGGTCTGGCCCCCATG-3′ |
| | Reverse: 5′-AGTCCACCATGGAGACATTCTCTC-3′ |
| OPN | Forward: 5′-GGGAAGCTCAGTGGAAGTAAAG-3′ |
| | Reverse: 5′-CTGCTGTGTCCCATGTTGTAT-3′ |
| BSP | Forward: 5′-TCACCTGTGCCATACCAGTTAA-3′ |
| | Reverse: 5′-TGAGATGGGTCAGGGTTTAGC-3′ |
| vWF | Forward: 5′-CTCCGTTTGACCGCAAAA-3′ |
| | Reverse: 5′-ACAGCAGGTGTCTCCGATCT-3′ |
| Ang-1 | Forward: 5′-CAGGAGGATGGTGGTTTGAT-3′ |
| | Reverse: 5′-TGCCACTTTATCCCATTCAG-3′ |
| β-actin | Forward: 5′-AGAGCTACGAGCTGCCTGAC-3′ |
| | Reverse: 5′-AGCACTGTGTTGGCGTACAG-3′ |

manufacturer's instructions. RT-qPCR primers (Table 1) were designed based on cDNA sequences from the NCBI Sequence database. SYBR Green qPCR Master Mix (Invitrogen) was used for detection and the target mRNA expressions were assayed on the ABI Step One Plus real-time PCR system (Applied Biosystems, Foster City, California, USA). Each sample was performed in triplicate.

### 2.9 Alizarin red S stain

The accumulated calcium deposition on the WJMSCs after 2 and 3 weeks of culturing in osteogenic differentiation medium was analyzed using Alizarin Red S staining, as developed in a previous study [25]. In brief, the specimens were fixed with 4% paraformaldehyde (Sigma-Aldrich) for 15 min and then incubated in 0.5% Alizarin Red S (Sigma-Aldrich) at a pH of 4.0 for 15 min at room temperature. After this, the cells were washed with PBS and photographs were taken using an optical microscope (BH2-UMA, Olympus, Tokyo, Japan) equipped with a digital camera (Nikon, Tokyo, Japan) at a 200x magnification. The Alizarin Red was also quantified using a solution of 20% methanol and 10% acetic acid in water. After 15 min, the liquid was transferred to a 96-well, and the quantity of Alizarin Red was determined using a spectrophotometer at 450 nm.

### 2.10 Statistical analysis

A one-way analysis of the variance statistical data was used to evaluate the significance of the differences between the means in the measured data. A Scheffé's multiple comparison test was used to determine the significance of the deviations in the data for each specimen. In all cases, the results were considered statistically significant with a $p$ value $< 0.05$.

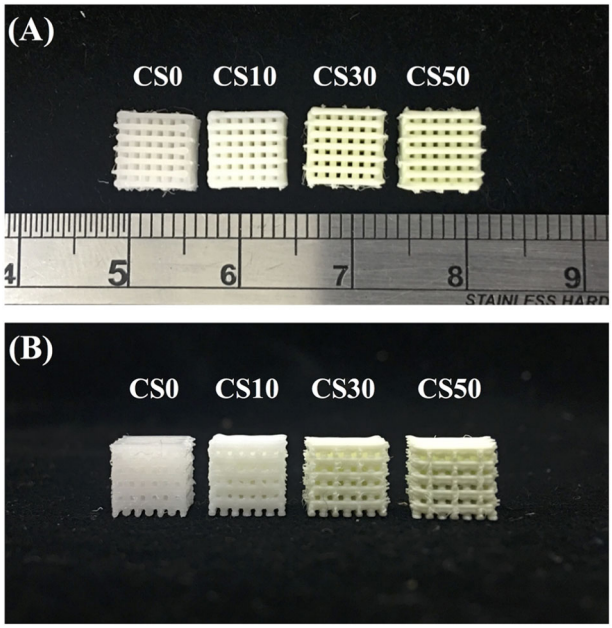


**Fig. 1** The photographs of (**a**) top view and (**b**) side view of different various CS/PCL scaffold

## 3 Results

### 3.1 The characterization of CS/PCL scaffolds

A layer-by-layer plotted CS/PCL scaffold in which 10, 30, and 50% CS mixed with PCL was fabricated. The scaffold showed a fully interconnected, well-defined pore morphology and porous structure. Photographs of the printed CS/PCL hybrid 3D-scaffold are shown in Fig. 1. The parameter of 3D-scaffolds was measured by 6.5 mm × 6.5 mm × 6.5 mm. When the content of CS is increased, the colour of the scaffold will gradually be yellowed from the original PCL white. The hydrophilic behavior of CS/PCL scaffolds were tested by measuring the contact angle as shown in Fig. 2. The effect of contact angle on the measurement time was tested by contacting the DMEM droplet for 20 min at room temperature. The time-dependent contact angles of CS0, CS10, CS30, and CS50 scaffold were measured. The contact angles have slightly decreased in each specimen within 20 min after deposition. The contact angle of prepared CS/PCL scaffolds could be decreased from 67.8 ± 3.8°, 62.7 ± 3.2°, 59.1 ± 2.1° and 0° with CS0, CS10, CS30 and CS50, respectively.

XRD patterns of CS/PCL composite scaffolds at various weight ratios are demonstrated in Fig. 3. Pristine PCL (CS0) showed the prominent crystalline peaks at $2\theta$ of 21° and

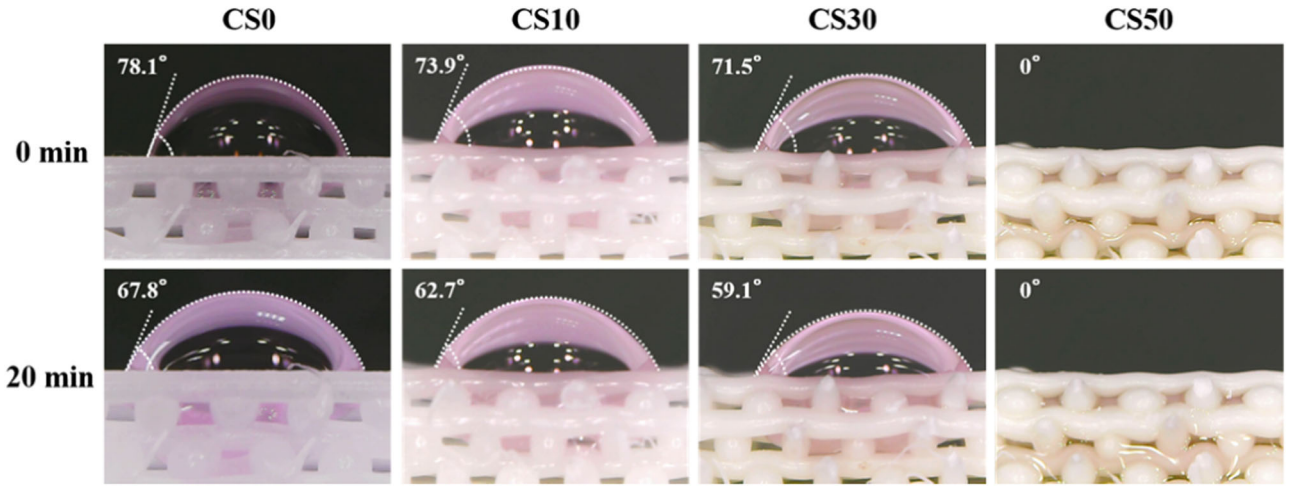


**Fig. 2** Water contact angle of different various CS/PCL scaffold

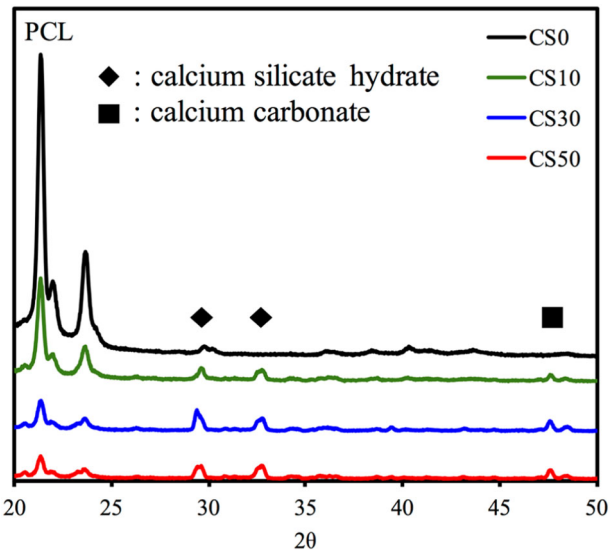


**Fig. 3** XRD patterns of the various CS/PCL scaffolds

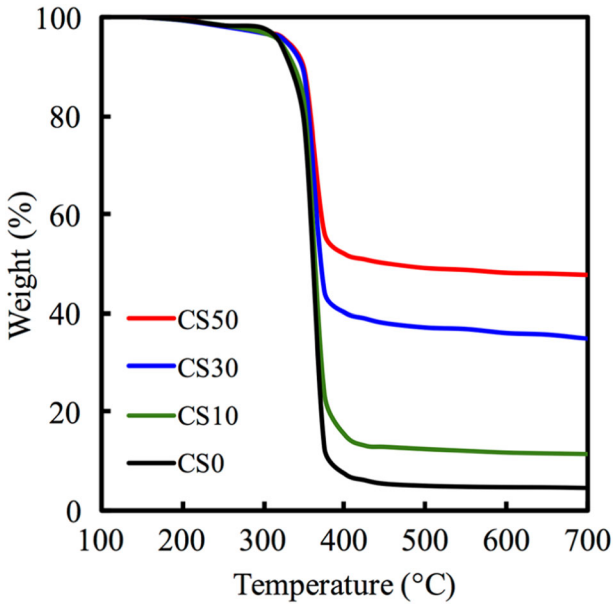


**Fig. 4** TGA curves of different CS/PCL scaffolds

23.5° [19]. These main characteristic peaks gradually decreased with the percentage of CS content increasing. Instead, the intensity of the diffraction peak of CS was found approximately at the range of $2\theta$ from 29° to 34° [25]. CS50 has an obvious diffraction peak near $2\theta = 29.4°$, which corresponds to the CSH gel, and incompletely reacted inorganic component phases of the β-dicalcium silicate (β-Ca2SiO4) at $2\theta$ between 32° and 34° [26]. In order to confirm the content of CS/PCL composites in Fig. 4, further presents the thermal weight loss curves from TGA. The samples have been heated at 10 °C/min up to 700 °C. The CS/PCL composite scaffold revealed two different weight losses stages. This can be observed that the first weight loss from the beginning of 100 °C was most likely stored water molecule in the composites. The second one between 350 to 420 °C was owing to pyrolysis of PCL, which provokes chain cleavages [8]. On account of high-temperature insulation of CS, our result showed that the CS remaining weight was consistent with the weight percentage used to blend with PCL. The CS50 had larger mineral crystal content than that of the CS30 and CS10 groups, with 47.9, 34.9, and 11.3% of their weights remaining, respectively [27].

Figure 5 shows the stress–strain curve for the different ratio of CS/PCL hybrid scaffolds with dimensions of 6.5 mm × 6.5 mm × 10 mm at a constant stretching velocity of 0.5 mm/s until deformation up to 20%. With increased in the amount of CS, the compressive strength of composite scaffold appeared significantly superior to those with the relatively lower proportion of CS, but the brittle behavior of

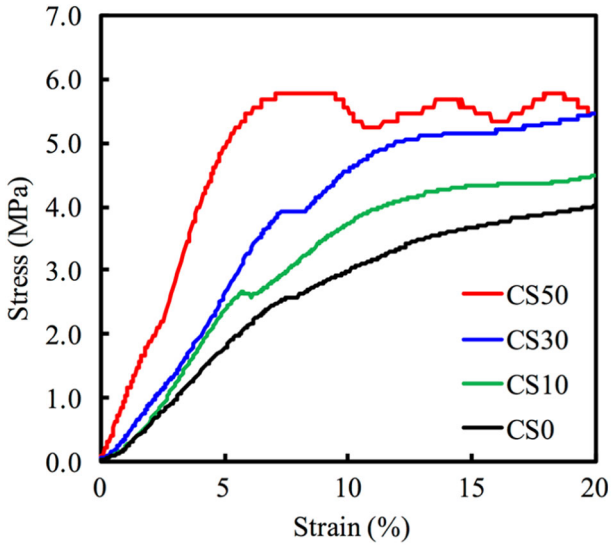


**Fig. 5** The strain-stress curves of different CS/PCL scaffolds

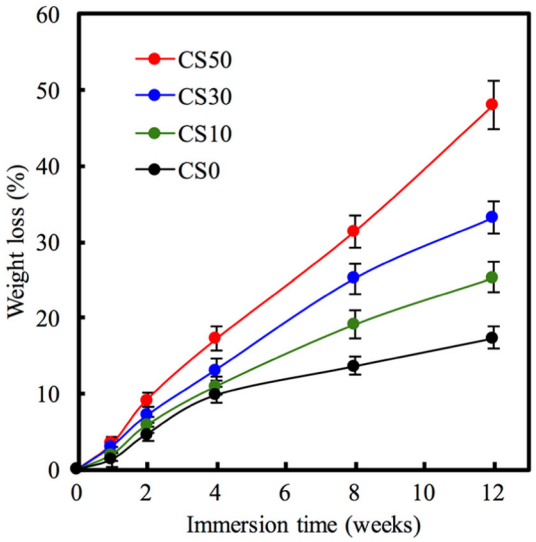


**Fig. 6** The weight loss of CS/PCL scaffolds immersed in SBF for different time-points

scaffold also increased due to the inherently poor tensile strength of CS. We supposed the increase in mechanical properties of the CS/PCL composites scaffolds, compared to PCL, can be attributed to the formation of CS agglomerates, which may result in the homogeneous dispersion of the inorganic filler into the PCL materials [28].

### 3.2 Bioactivity

Figure 6 represents the PCL and CS/PCL scaffolds weight loss in SBF solution at 37 °C throughout the 12 weeks of degradation. The weight loss of all specimens was similar at the beginning of immersion time. The degradation rate of all CS/PCL scaffolds rapidly increased for the first 2 weeks and reached a maximum after 12 weeks. As the soaking time increased, the weight loss of the specimens raised from the observed data. In addition, the scaffold with highest CS level compared with others had the faster dissolution rate attributed to the hydrolysis of calcium silicate, and their weight loss of CS0, CS10, CS30, and CS50 percentage were about 16, 24, 32, and 49%, respectively. SEM was utilized to analyze the morphology and microstructure of the 3D scaffolds. The images of the scaffolds' surface before and after immersion in SBF for 7 days were shown in Fig. 7. As can be seen, the pure PCL (CS0) retained a smooth and dense surface during the soaking time-points. On the contrary, the scaffold with 10–50 wt% CS had affection for it after immersion for 1 day in SBF, miniature globular particles were spread all over the surfaces which were formed of apatite precipitates.

### 3.3 Ion release

The profiles of Ca, Si, Mg and P ion concentrations in various immersing time in SBF are shown in Fig. 8. SBF solution contained Ca and P ions which form a calcified bone-like apatite layer through direct contact with the surface of 3D scaffolds that caused drops of the Ca and P concentration as it can be seen in the Fig. 8a, d. Also, this trend indicates that the higher the proportion of CS content, the more HA formed on the surface of the material and the findings can be more easily observed next in the SEM micrographs. In contrast, Fig. 8b shows Si ions release amount increased with increasing the proportion of CS at each measurement time point. The Si ion concentrations of CS0, CS10, CS30, and CS50 immersed in SBF for 12 weeks were 0.00, 0.71, 1.11 and 1.61 mM, respectively. The CS-contained scaffolds doped with Mg ion continuously released for 12 weeks at a steady rate. The Mg ion released from CS50 was 1.18, 1.40, 1.51, 1.60 mM after immersed for 1, 4, 8, and 12 weeks, respectively.

### 3.4 Cell adhesion and proliferation

The adhesion and proliferation behaviors of WJMSC on 3D-printed CS/PCL scaffolds were measured for up to 7 days' incubation and shown in Fig. 9. Lacking in hydrophilic environment of CS0 (PCL) led to the worst outcome in our case. The adhesion of WJMSC shown in Fig. 9a indicates that adhered cell on the 3D scaffolds were more than 90% of Ctl in the first 6 h. Still, with increasing the concentration of CS, the cell proliferation and viability was higher than that on CS0 and the Ctl, indicating that CS could be used as a promising bioactive material to enhance biocompatibility. The cell adhesion ability can be inhibited

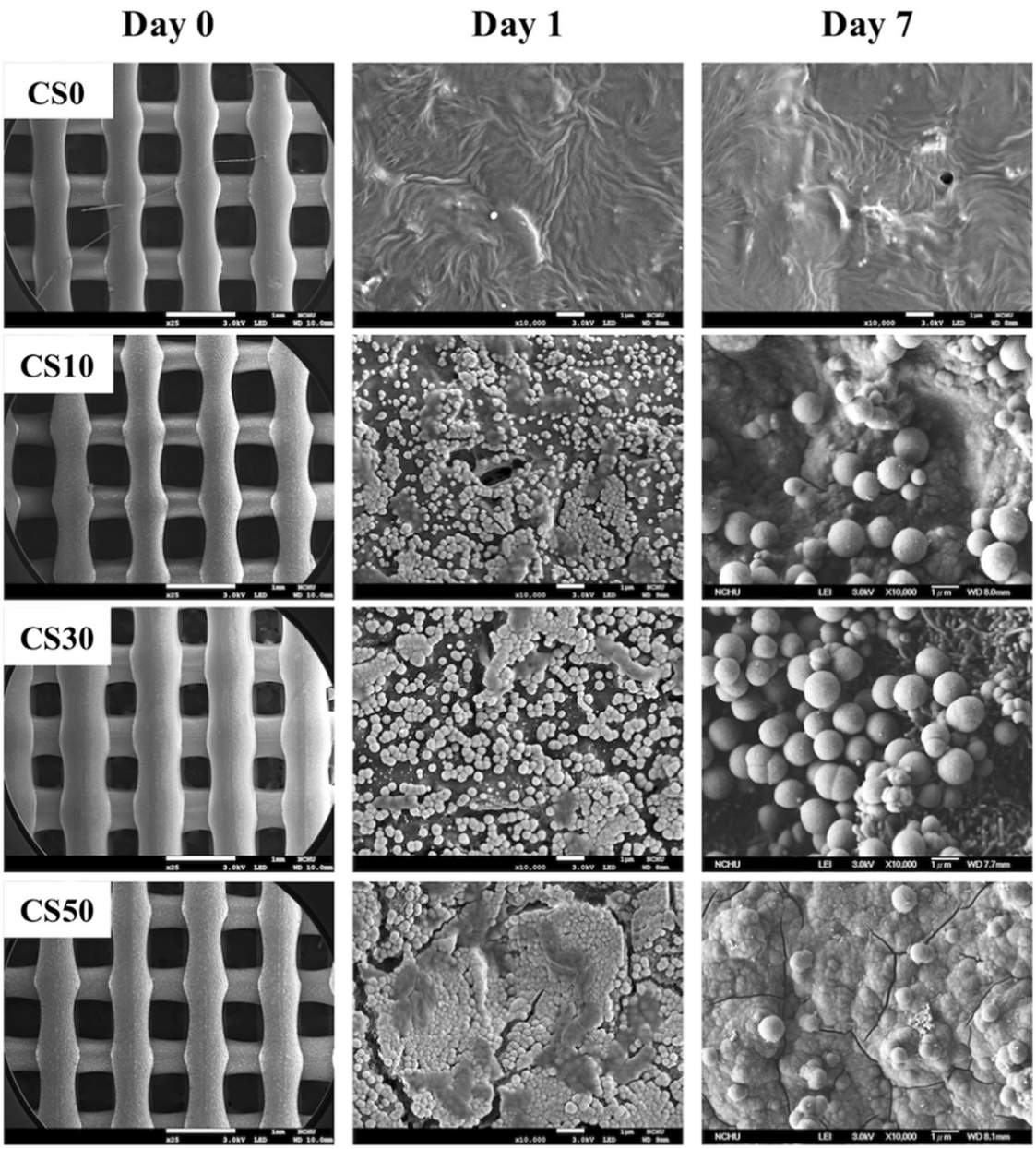


**Fig. 7** Surface SEM images of the CS/PCL scaffolds before and after immersion in SBF

if cultured on material with hydrophobic, while a scaffold contained CS are extremely hydrophilic [29]. After 7 days of culture, the quantitative analysis showed that the proliferation of WJMSC cultured on CS50 was significantly higher than that of the CS0 (1.22 fold), CS10 (1.15 fold) and CS30 (1.07 fold) groups (Fig. 9b).

Fluorescent staining of WJMSC adhesion on CS/PCL scaffolds during 7 days of culture was examined in our study (Fig. 10). After 1 day of incubation, it is obviously seen that green fluorescence of cells appeared in round-shaped at CS0 and CS10. The morphology of cells altered gradually during the experimental period; however, stellate-shaped cells with widespread cytoplasm were investigated on day 7. When the WJMSC were seeded onto the CS0, CS10, CS30 and CS50 matrices for 3 h, the cellular response on the CS50 matrices was significantly spread out higher than on the others, whereas the cells cultured on the others exhibited with round cells (Fig. 11). Even more, cell attachment and spreading of CS50 showed the best results until the 7 d.

### 3.5 Cell differentiation

To quantitatively determine the osteogenic-related and angiogenesis-related gene expression, the western blotting analysis also has been carried out on CS0, CS10, CS30, and

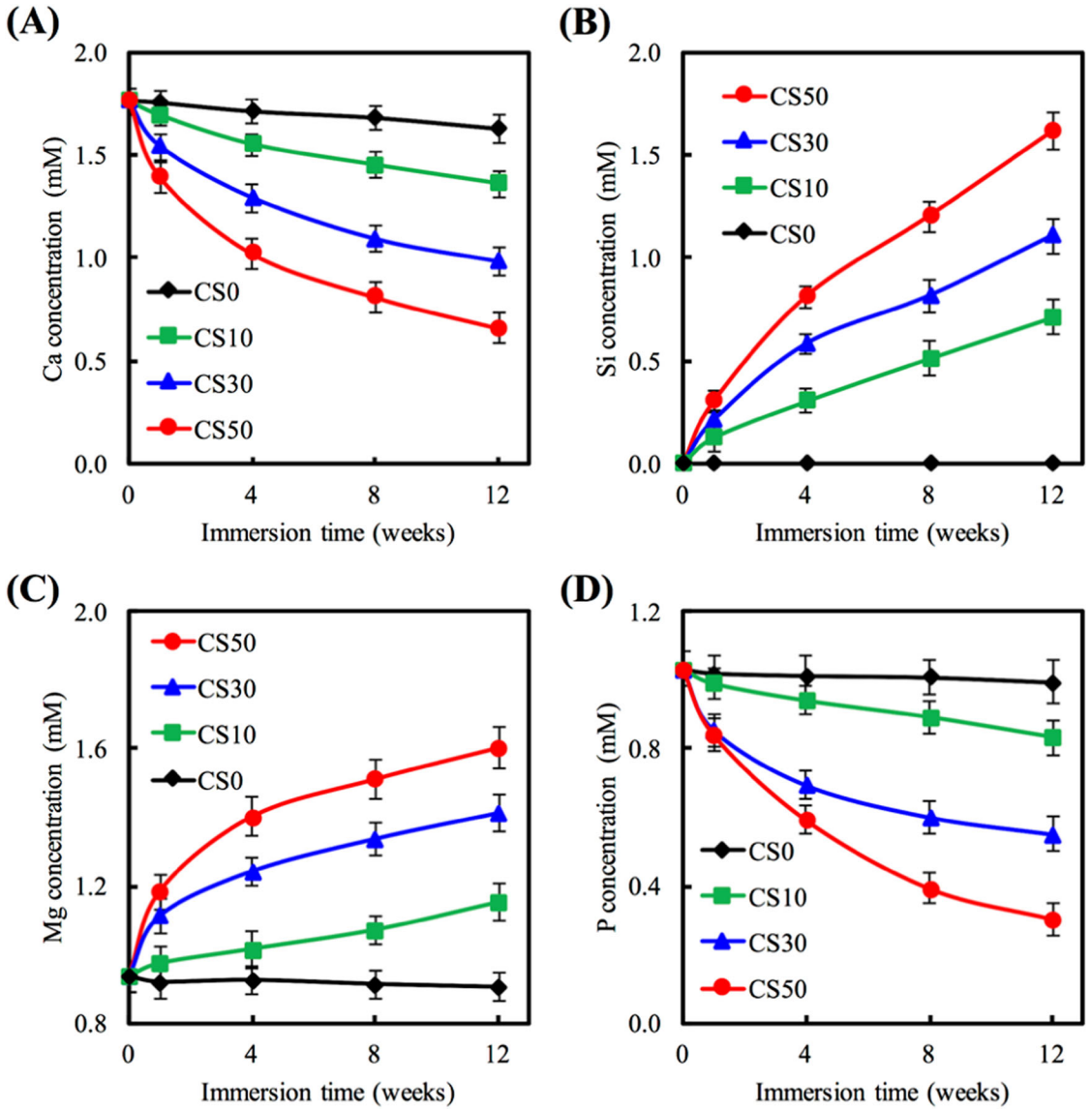


**Fig. 8** **a** Ca, **b** Si, **c** Mg and **d** P ions concentration of SBF after CS/PCL scaffolds soaking for different times

CS50 scaffolds. The expression of osteogenic-related proteins, ALP and OPN, has been commonly regarded as a biomarker for characterizing bone turnover in the early stage, and the marker of OC in the late stage as well. And the late osteogenesis markers such as OCN were greatly increased in CS30 and CS50 compared with CS10, suggesting the synergistic effects were observed in biochemical assays for ALP activity and calcium production. These finding were further confirmed by mineral deposition. In addition, vWF and Ang-1 have been described as an essential regulator which is involved in multiple vascular processes. As seen in Fig. 12, the total protein levels in all CS groups were significantly enhanced which is indicated with * at $p < 0.05$ when compared to samples in the absence of CS (Ctl/CS0). In vitro Alizarin Red S staining (Fig. 13) evidently indicated that WJMSC cultured in CS/PCL scaffolds showed significantly greater calcium mineral content after 2 and 3 weeks than on WJMSC cultured on bare scaffold (CS0). The results revealed that the ARS-stained CS0 scaffolds shown pink-pale red color regardless of the culture periods. The extent of mineralization along with the different struts ranging from light pink to brick red were able to visually examined through optical colorimetry. After 3 weeks, the quantitative analysis demonstrated that the level of deposited calcium of cells cultured on the CS50 were 1.81, 1.52, and 1.13 times higher than that on CS0, CS10, and CS30 ($p < 0.05$), respectively. These results illustrate that the CS/PCL scaffolds might exhibit the ability to stimulate the mineralization of WJMSC.

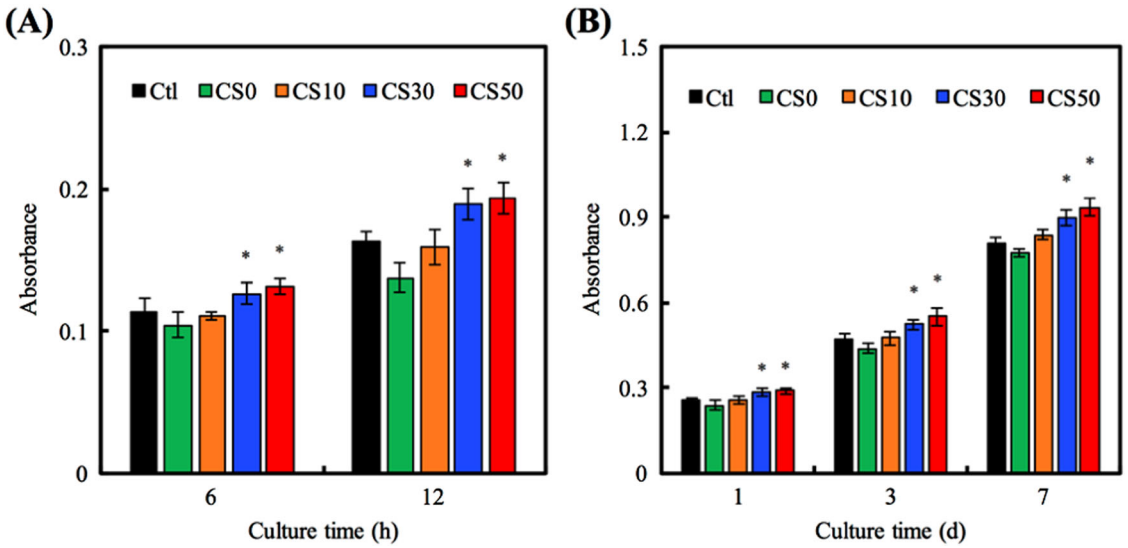


**Fig. 9** **a** Adhesion and **b** proliferation of WJMSC cultured on CS/PCL scaffolds for different time points. Asterisk indicates a significant difference ($p < 0.05$) compared to CS0

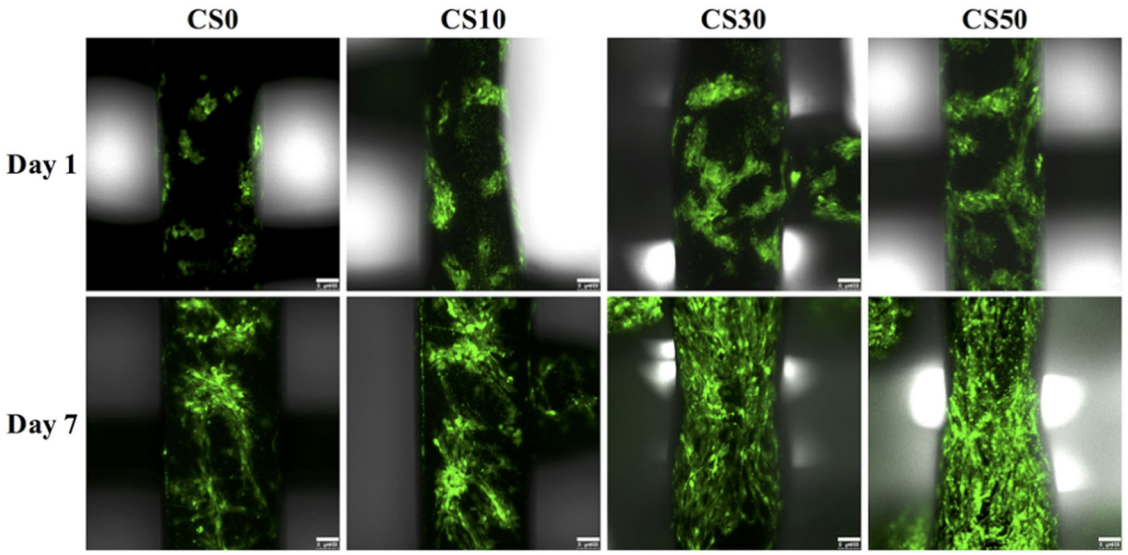


**Fig. 10** The immunofluorescence of WJMSC cultured on CS/PCL scaffolds for 1 and 7 days

## 4 Discussion

Recently, the calcium silicate-based materials had attracted various attention for the application in hard tissue regeneration due to their excellent bioactivity [30, 31]. In order to consider the performance of bioactive calcium silicate/PCL composite scaffold and the physiological function was employed to manufacture a novel 3D-printed bioceramic scaffold in this study. In addition, we have incorporated various concentrations of CS into PCL, with the aim of developing a printable, mechanically strong, and biodegradable material while avoiding the use of organic solvents.

Wettability plays a key role in determining the biological behavior of the biomaterial and thus making it a critical consideration factor when designing implant materials [29]. Cellular behaviours were enhanced when they were grown on specimens with a water contact angle that was lower than 75°. The largest spreading occurs in CS50 surface after droplet exposure, which implies that the higher CS ratio is in charge of the better hydrophilic property. In other words, the hydrophilicity of the scaffolds was further significantly

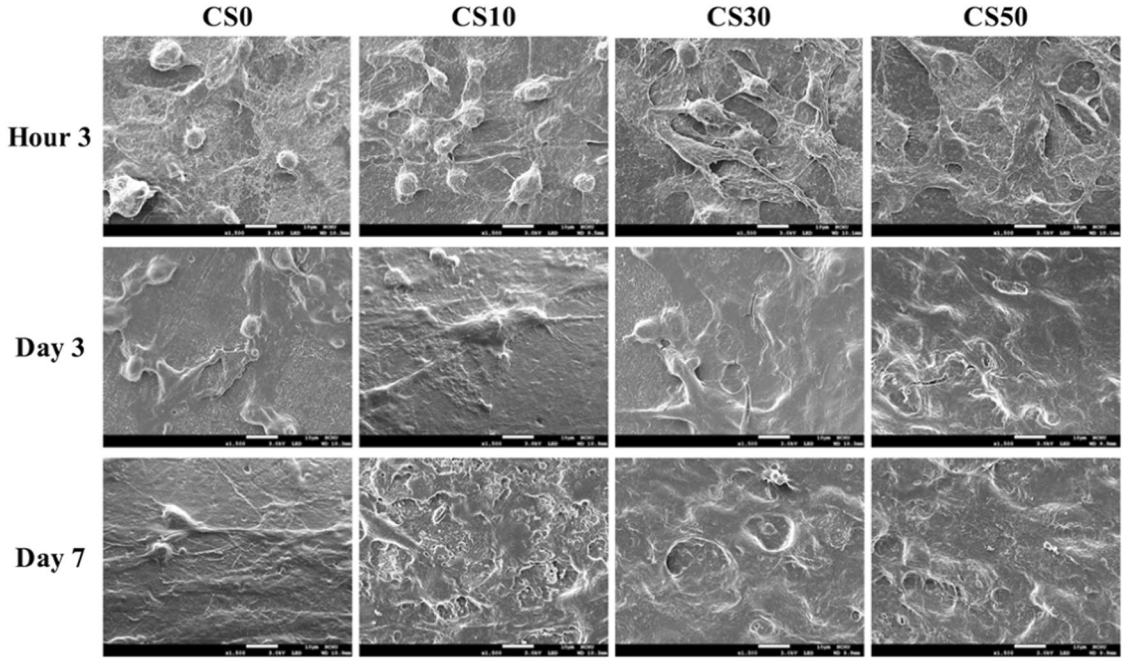


**Fig. 11** The SEM of WJMSC cultured on CS/PCL scaffolds for 3 h, 3 days, and 7 days

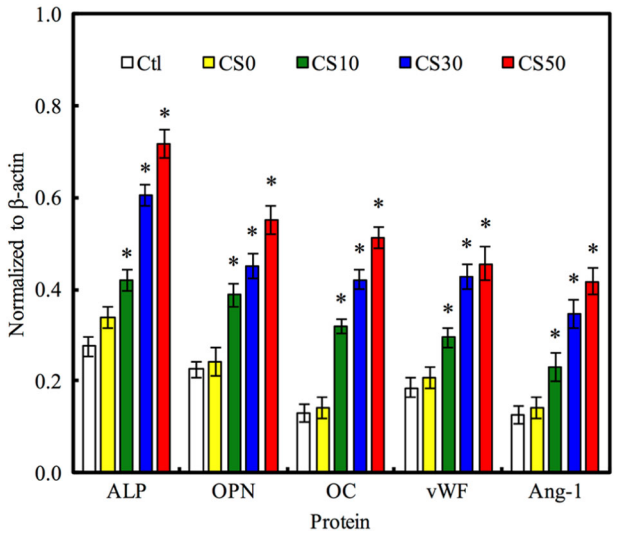


**Fig. 12** The gene expression in the WJMSC were cultured on CS/PCL scaffolds for 7 days. Asterisk indicates a significant difference ($p < 0.05$) compared to CS0

increased after we additive CS into PCL as the DMEM infiltrated into the material right after it came into contact with the scaffolds. The suitable range of contact angles for implanted substrates is lower than 40°, with 0° being totally hydrophilic. The cell behavior can be enhanced if grown on substrates with a water contact angle in this range; the data show that pure PCL scaffolding is hydrophobic, while a scaffold contained CS are extremely hydrophilic [29].

It is known that for hard tissue regeneration, the bioactive material with different bioactivity and degradation rate are needed used in the clinical [3]. The ideal maximum weight loss for each scaffold was calculated by assuming that the measured weight loss is due to (i) all of the bioactive CS in the composite and (ii) no weight loss is attributable to the degradation of PCL [32]. Therefore, the degradation rate of the 3D CS/PCL scaffold could be influenced to a certain extent by varying CS-contained effect, depending on the clinical needs [32]. The precipitated of the bone-like apatite on scaffold surface has proven to be useful in predicting the bone-bonding behavior of bone substitutes in vitro [10]. The CS template provided numerous favourable active nucleus sites induced growth of new apatite-like precipitates and deposition of HA [33]. There were few apatite spheres precipitate on CS10 and CS30 surface with an average size of less than 1 μm after immersed for day. However, CS50 was uniformly covered with spherical aggregated minerals. As reported in a previous study [34–36], Ca ions released from CS-based substrates possibly originating from the less-ordered hydration products that promoted significantly apatite growth by increasing local Ca concentration, thereby raising the ionic product of the apatite in the surrounding environment and enhancing the nucleation behavior of the apatite [9]. The apatite formation on the CS-based scaffolds surface contained release of Ca ion from the scaffolds and the Si-OH hydrate supplied favourable sites for apatite nucleation [37]. The main phenomenon could be attributed to the accessibility nucleation sites for the silicates. When the soaking

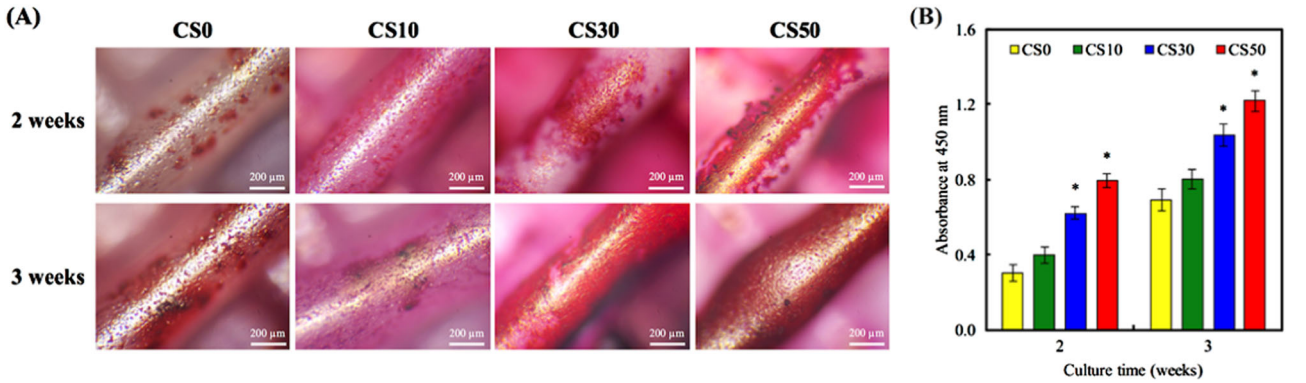


**Fig. 13** **a** Alizarin Red S staining and **b** quantification analysis of calcium nodules deposited on the CS/PCL scaffolds cultured with WJMSC for different time periods ($n = 5$). Astersisk indicates a significant difference ($p < 0.05$) compared to CS0

time reached to day 7, sustained formation of covered apatite layers was getting thicker, especially in the specimen of CS50.

Several studies provided the CS-based materials not only with excellent bioactivity [12], but also promoted osteogenesis and angiogenesis of primary cells [3, 38]. In addition, there were several studies proved Mg ions play an important role in stimulating cell behavior, which can enhance DNA and protein synthesis and regulate Mg conducting channels [39]. In brief, the bone incorporates various nutrients in the form of trace elements and both Si and Mg have been found to play absolutely vital roles during bone regeneration processes and they are essential cofactors for enzymes which involve in the synthesis of the constituents of bone matrix [40]. The cell adhesion ability can be inhibited if cultured on material with hydrophobic, while a scaffold contained CS are extremely hydrophilic [29]. However, the cells were more distributed homogeneously especially throughout the CS50 scaffolds which indicated the WJMSC to sense the microenvironment and to enhance cell behavior [41].

The stimulatory and dose-dependent proliferation effects of Si and Mg ionic products have been well-proven in various studies [10]. Shie et al. reported that the ion concentration of Si of 1 mM in cell culture medium increased the proliferation of osteoblast-like cell [42]. Chen et al. proved that the extract medium contained Si and Mg ions (ion concentrations of 1.06 mM and 1.03 mM, respectively) from Ca-Si-Mg cements elicited a stimulatory effect on the cementogenesis and angiogenesis differentiation of human periodontal ligament cells [24]. In this study, it was found that the Si and Mg ions concentrations were 0.22 mM and 1.12 mM released from CS30 after 7 days that almost similar to the previous studies [10]. Hence, we suggested the Si and Mg ions with certain concentration released from CS30 and CS50 scaffolds enhanced the adhesion and proliferation of WJMSC cells. In addition, many studies have demonstrated that Si ions play an important role in stimulating the osteogenic differentiation, and in inducing the formation of new bone [43]. In previous study, we proved the CS-based materials were promoted integrin-mediated cell adhesion and activate the osteogenesis signaling pathway by up-regulating the expression of focal adhesion kinase (FAK) and MAPE/ERK [42]. Thus, the CS50 may be due to altered ECM adsorption and biomineralization on scaffold surface, which may affect osteogenesis differentiation [15]. Several studies reported that Si is directly involved in the regeneration process of bone formation and mineralization [44]. The ionic products from 3D-printed CS-based scaffold significantly affected the proliferation, ALP and osteogenic-related gene expression of bone marrow stem cells [23]. It is found that several silicate-contained biomaterials with different component could promote the in vitro and in vivo osteogenesis differentiation of various types cells [45, 46]. Our results confirmed our previous finding with main components on CS-based ceramic and suggested that 3D-printed CS scaffolds are good candidates for hard tissue-regeneration applications.

## 5 Conclusions

In this work, we have demonstrated the novel CS-based material blended with PCL was developed by the solvent-free processing to conquer the limitation of biological behavior and fabricated the ideal porous 3D scaffold with adequate pore morphology and pore size for bone tissue engineering. Our results demonstrate that the 3D CS scaffold not only increases in mechanical properties but also provide suitable highly hydrated tissue-like microenvironments to support WJMSC adhesion and proliferation. Moreover, osteogenic and angiogenesis differentiation of WJMSC were further highly improved, thus making them emerging for regenerative medicine applications in the future. Our results would assist the fabricated of 3D

scaffolds with increased bioceramic leading to more robust or greater range of biological behaviors.

**Acknowledgements** The authors acknowledge receipt grants from the Ministry of Science and Technology (MOST 106-3114-E-039-001) and China Medical University Hospital grants (DMR-107-074).

**Compliance with ethical standards**

**Conflict of interest** The authors declare that they have no conflict of interest.

## References

1. Barui S, Chatterjee S, Mandal S, Kumar A, Basu B. Microstructure and compression properties of 3D powder printed Ti-6Al-4V scaffolds with designed porosity: experimental and computational analysis. Mater Sci Eng C Mater Biol Appl. 2017;70:812–23.
2. Bertol LS, Schabbach R, Loureiro Dos, Santos LA Different post-processing conditions for 3D bioprinted α-tricalcium phosphate scaffolds. J Mater Sci Mater Med. 2017;28:168.
3. Su CJ, Tu MG, Wei LJ, Hsu TT, Kao CT, Chen TH, et al. Calcium silicate/chitosan-coated electrospun poly (lactic acid) fibers for bone tissue engineering. Materials. 2017;10:501.
4. Wang X, Ao Q, Tian X, Fan J, Wei Y, Hou W, et al. 3D bioprinting technologies for hard tissue and organ engineering. Materials. 2016;9:802.
5. Shie MY, Chang WC, Wei LJ, Huang YH, Chen C-H, Shih CT, et al. 3D printing of cytocompatible water-based light-cured polyurethane with hyaluronic acid for cartilage tissue engineering applications. Materials. 2017;10:136.
6. Kao CT, Lin CC, Chen YW, Yeh CH, Fang HY, Shie MY. Poly (dopamine) coating of 3D printed poly(lactic acid) scaffolds for bone tissue engineering. Mater Sci Eng C Mater Biol Appl. 2015;56:165–73.
7. Chiu YC, Fang HY, Hsu TT, Lin CY, Shie MY. The characteristics of mineral trioxide aggregate/polycaprolactone 3-dimensional scaffold with osteogenesis properties for tissue regeneration. J Endod. 2017;43:923–9.
8. Huang SH, Hsu TT, Huang TH, Lin CY, Shie MY, Fabrication and characterization of polycaprolactone and tricalcium phosphate composites for tissue engineering applications. J Dent Sci. 2017;12:33–43.
9. Ho CC, Fang HY, Wang B, Huang TH, Shie MY, The effects of Biodentine/polycaprolactone 3D-scaffold with odontogenesis properties on human dental pulp cells. Int Endod J. 2017. https://doi.org/10.1111/iej.12799.
10. Chen YW, Hsu TT, Wang K, Shie MY. Preparation of the fast setting and degrading Ca-Si-Mg cement with both odontogenesis and angiogenesis differentiation of human periodontal ligament cells. Mater Sci Eng C Mater Biol Appl. 2016;60:374–83.
11. Shen YF, Ho CC, Shie MY, Wang K, Fang HY. Hinokitiol-loaded mesoporous calcium silicate nanoparticle induce apoptotic cell death through regulation of the function of MDR1 in lung adenocarcinoma cells. Materials. 2016;9:306.
12. Shie MY, Chiang WH, Chen IWP, Liu WY, Chen YW. Synergistic acceleration in the osteogenic and angiogenic differentiation of human mesenchymal stem cells by calcium silicate–graphene composites. Mater Sci Eng C Mater Biol Appl. 2017;73:726–35.
13. Zhai D, Xu M, Liu L, Chang J, Wu C, Silicate-based bioceramics regulating osteoblast differentiation through a BMP2 signalling pathway. J Mater Chem B. 2017;5:7297–306.
14. Chou MY, Kao CT, Hung CJ, Huang TH, Huang SC, Shie MY, et al. Role of the p38 pathway in calcium silicate cement-induced cell viability and angiogenesis-related proteins of human dental pulp cell in vitro. J Endod. 2014;40:818–24.
15. Shie MY, Ding SJ. Integrin binding and MAPK signal pathways in primary cell responses to surface chemistry of calcium silicate cements. Biomaterials. 2013;34:6589–606.
16. Chen YW, Ho CC, Huang TH, Hsu TT, Shie MY, The ionic products from mineral trioxide aggregate–induced odontogenic differentiation of dental pulp cells via activation of the Wnt/β-catenin signaling pathway. J Endod. 2016;42:1062–9.
17. Hinton TJ, Hudson A, Pusch K, Lee A, Feinberg AW, 3D printing PDMS elastomer in a hydrophilic support bath via freeform reversible embedding. ACS Biomater Sci Eng. 2016;2:1781–6.
18. Huang A, Jiang Y, Napiwocki B, Mi H, Peng X, Turng L-S, Fabrication of poly(ε-caprolactone) tissue engineering scaffolds with fibrillated and interconnected pores utilizing microcellular injection molding and polymer leaching. RSC Adv. 2017;7:43432–44.
19. Tsai KY, Lin HY, Chen YW, Lin CY, Hsu TT, Kao CT. Laser sintered magnesium-calcium silicate/poly-ε-caprolactone scaffold for bone tissue engineering. Materials. 2017;10:65.
20. Liu W, Wang D, Huang J, Wei Y, Xiong J, Zhu W, et al. Low-temperature deposition manufacturing: a novel and promising rapid prototyping technology for the fabrication of tissue-engineered scaffold. Mater Sci Eng C Mater Biol Appl. 2017;70:976–82.
21. Yu GZ, Chou D-T, Hong D, Roy A, Kumta PN, Biomimetic rotated lamellar plywood motifs by additive manufacturing of metal alloy scaffolds for bone tissue engineering. ACS Biomater Sci Eng. 2017;3:648–57.
22. Wang Di, Wang Y, Wang J, Song C, Yang Y, Zhang Z, et al. Design and fabrication of a precision template for spine surgery using selective laser melting (SLM). Materials. Multidiscip Digit Publ Inst. 2016;9:608.
23. Zhu H, Zhai D, Lin C, Zhang Y, Huan Z, Chang J, et al. 3D plotting of highly uniform Sr5(PO4)2SiO4 bioceramic scaffolds for bone tissue engineering. J Mater Chem B. 2016;4:6200–12.
24. Chen YW, Yeh CH, Shie MY. Stimulatory effects of the fast setting and degradable Ca–Si–Mg cement on both cementogenesis and angiogenesis differentiation of human periodontal ligament cells. J Mater Chem B. 2015;3:7099–108.
25. Huang MH, Shen YF, Hsu TT, Huang TH, Shie MY. Physical characteristics, antimicrobial and odontogenesis potentials of calcium silicate cement containing hinokitiol. Mater Sci Eng C Mater Biol Appl. 2016;65:1–8.
26. Huang MH, Kao CT, Chen YW, Hsu TT, Shieh DE, Huang TH, et al. The synergistic effects of chinese herb and injectable calcium silicate/b-tricalcium phosphate composite on an osteogenic accelerator in vitro. J Mater Sci Mater Med. 2015;26:161.
27. Kung FC, Lin CC, Lai WFT. Osteogenesis of human adipose-derived stem cells on hydroxyapatite-mineralized poly(lactic acid) nanofiber sheets. Mater Sci Eng C Mater Biol Appl. 2014;45:578–88.
28. Gómez-Lizárraga KK, Flores-Morales C, Del Prado-Audelo ML, Álvarez-Pérez MA, Piña-Barba MC, Escobedo C. Poly-caprolactone- and polycaprolactone/ceramic-based 3D-bioplotted porous scaffolds for bone regeneration: a comparative study. Mater Sci Eng C Mater Biol Appl. 2017;79:326–35.
29. Cheng YL, Chen YW, Wang K, Shie MY, Enhanced adhesion and differentiation of human mesenchymal stem cell inside apatite-mineralized/poly(dopamine)-coated poly(ε-caprolactone) scaffolds by stereolithography. J Mater Chem B. 2016;4:6307–15.

30. Ye X, Leeflang S, Wu C, Chang J, Zhou J, Huan Z. Mesoporous bioactive glass functionalized 3D Ti-6Al-4V scaffolds with improved surface bioactivity. Materials. 2017;10:1244.
31. Chen YC, Shie MY, Wu YH, Lee KX, Wei LJ, Shen YF, Anti-inflammation performance of curcumin-loaded mesoporous calcium silicate cement. J Formos Med Assoc. 2017;116:679–88.
32. Mohammadkhah A, Marquardt LM, Sakiyama-Elbert SE, Day DE, Harkins AB. Fabrication and characterization of poly-(ε)-caprolactone and bioactive glass composites for tissue engineering applications. Mater Sci Eng C Mater Biol Appl. 2015;49:632–9.
33. Lai WY, Chen YW, Kao CT, Hsu TT, Huang TH, Shie MY. Human dental pulp cells responses to apatite precipitation from dicalcium silicates. Materials. 2015;8:4491–504.
34. Mehrali M, Moghaddam E, Shirazi SFS, Baradaran S, Mehrali M, Latibari ST, et al. Synthesis, mechanical properties, and in vitro biocompatibility with osteoblasts of calcium silicate-reduced graphene oxide composites. ACS Appl Mater Interfaces. 2014;6:3947–62.
35. Liu CH, Huang TH, Hung CJ, Lai WY, Kao CT, Shie MY. The synergistic effects of fibroblast growth factor-2 and mineral trioxide aggregate on an osteogenic accelerator in vitro. Int Endod J. 2014;47:843–53.
36. Zancanela DC, de Faria AN, Simao AMS, Gonçalves RR, Ramos AP, Ciancaglini P. Multi and single walled carbon nanotubes: effects on cell responses and biomineralization of osteoblasts cultures. J Mater Sci Mater Med. 2016;27:62.
37. Liu X, Ding C, Chu PK. Mechanism of apatite formation on wollastonite coatings in simulated body fluids. Biomaterials. 2004;25:1755–61.
38. Huang CY, Huang TH, Kao CT, Wu YH, Chen WC, Shie MY. Mesoporous calcium silicate nanoparticles with drug delivery and odontogenesis properties. J Endod. 2017;43:69–76.
39. Abed E, Moreau R. Importance of melastatin-like transient receptor potential 7 and magnesium in the stimulation of osteoblast proliferation and migration by platelet-derived growth factor. Am J Physiol Cell Physiol. 2009;297:C360–8.
40. Jugdaohsingh R, Pedro LD, Watson A, Powell JJ. Silicon and boron differ in their localization and loading in bone. Bone Rep. 2015;1:9–15.
41. Gu Z, Wang S, Weng W, Chen X, Cao L, Wei J, et al. Influences of doping mesoporous magnesium silicate on water absorption, drug release, degradability, apatite-mineralization and primary cells responses to calcium sulfate based bone cements. Mater Sci Eng C Mater Biol Appl. 2017;75:620–8.
42. Shie MY, Ding SJ, Chang HC. The role of silicon in osteoblast-like cell proliferation and apoptosis. Acta Biomater. 2011;7:2604–14.
43. Yang C, Wang X, Ma B, Zhu H, Huan Z, Ma N, et al. 3D-printed bioactive Ca3SiO5 bone cement scaffolds with nano surface structure for bone regeneration. ACS Appl Mater Interfaces. 2017;9:5757–67.
44. Mao L, Xia L, Chang J, Liu J, Jiang L, Wu C, The synergistic effects of Sr and Si bioactive ions on osteogenesis, osteoclastogenesis and angiogenesis for osteoporotic bone regeneration. Acta Biomater. 2017;61:217–32.
45. Fuh LJ, Huang Y-J, Chen WC, Lin DJ. Preparation of microporous bioceramic containing silicon-substituted hydroxyapatite and beta-tricalcium phosphate. Mater Sci Eng C Mater Biol Appl. 2017;75:798–806.
46. Rathinam E, Rajasekharan S, Chitturi RT, Declercq H, Martens L, De Coster P. Gene expression profiling and molecular signaling of various cells in response to tricalcium silicate cements: a systematic review. J Endod. 2016;42:1713–25.